Deformation of Small Droplets at High Weber Number

Vasco O. Duke-Walker[1], Calvin J. Young[1], Manoj Paudel[1], Stephan Agee[1], Jacob Keltz[1]
Letice Bussiere[2], Prashant Tarey[2], Praveen Ramaprabhu[2], and Jacob A. McFarland[1] *

1. Department of Mechanical Engineering
Texas A&M University College Station, TX 77840 USA

2. Department of Mechanical Engineering and Engineering Science
University of North Carolina at Charlotte Charlotte, NC 28223 USA

Abstract

Droplet breakup is a complex process involving interfacial instability and transport across a wide range of length and time scales. Fundamental studies of shock-droplet interaction provide valuable insight into the physical processes behind droplet breakup at high Weber and Reynolds numbers. Many high-speed applications such as liquid-fueled detonations and hypersonic hydrometeor impacts involve small droplets under high Weber numbers and/or unsteady conditions. The work presented here will explore deformation and hydrodynamics leading to breakup for small droplets ($< 200\mu m$) at high Weber numbers. An experimental campaign is presented whereby droplet deformation is measured at high temporal and spatial resolution. Small rapidly evaporating droplets ($\approx 150\mu m$) at Weber numbers in excess of 1000 are studied. High-speed (sub-microsecond image times) shadowgraphy provides measurement of the droplet deformation rate, acceleration, and breakup timing. DNS results are presented to further explore deformation rates for smaller droplets ($\approx 5\mu m$). Deformation rates are compared with existing models for both experimental and simulation cases. This ongoing work will provide additional data from which our understanding of complex droplet phenomena may be advanced and applied to physical systems.

*Corresponding Author: vascoduke@tamu.edu & mcfarlandja@tamu.edu

Introduction

Shock droplet interactions are encountered in a broad range of engineering systems. A droplet may be exposed to bow shocks, blast waves, and detonations in any number of configurations and scales. The performance of these systems relies on the ability to model the temporal and spatial evolution of droplets exposed to shockwaves and high speed flows. The evolution of the droplet begins with deformation, driving the initial acceleration, and altering the morphology of the parent droplet interface. In some applications, e.g. hypersonic hydrometeor impacts, deformation may be the only phase of evolution before the process is terminated by an impact. Thus, a thorough understanding of the droplet deformation processes is necessary to understand the subsequent hydrodynamics and breakup.

Aerodynamic droplet breakup may be thought of as a process where the aerodynamic forces acting on the surface of a droplet surpass the interstitial surface tension force resisting deformation, resulting in unstable deformation and eventual breaking of a parent droplet into child droplets. Breakup and deformation processes are commonly characterized by the Weber number $We = \frac{\rho_g u^2 d_p}{\sigma}$, the ratio of inertial forces acting over the surface area of a droplet to the interstitial surface tension. Various morphologies of deformation and breakup have been observed for different Weber number regimes, though generally for $We < 1000$. At higher Weber numbers encountered in many systems of interest, the droplet breakup process is expected to be in the shear stripping, or catastrophic breakup regimes [1].

Studies on droplet breakup typically generate high Weber numbers by increasing the particle size rather than the velocity of the free gas stream, often for practical reasons such as the limitation of high-Mach number shock tubes, or low-rate data acquisition systems. While these studies may achieve variations in Weber number, it is crucial to distinguish that smaller droplets accelerate and equilibrate with the flow faster than larger ones, and that the pressure gradient and relative gas velocity in high Mach flows is larger. These experimental discrepancies in the freestream conditions about the droplet raise the question of whether the hydrodynamics that drive breakup in larger ($> 1mm$) droplets also drive the process in smaller $O(100\mu m)$ droplets. Experimentally quantifying the discrepancy in behavior across diameters is crucial, as variations in droplet drag due to deformation may significantly impact droplet lag times and trajectories in Euler-Lagrange simulations.

In this study, a high We droplet deformation regime is investigated for small droplets through experiment and simulation, with comparison to relevant models. Shock tube experiments with high-speed and high-magnification shadowgraphy are conducted to collect data on the time evolution of droplet deformation morphology with high accuracy. The parameters in the experiments have been selected to provide a comparison with experimental and numerical work presented in the literature for similar Weber number regimes at different droplet sizes, e.g. the work by Mizuno [2] with 2.33 mm droplets at $We \sim 100 - 2000$, and Poplavski [3] over similar conditions. Simulations of fully resolved droplets undergoing deformation and breakup are conducted for smaller droplets at similar We and higher Mach numbers. The results are compared to the predictions of several extant models to assess their ability at modelling the behavior of small droplets. This work serves to bridge the gap in understanding in the nature of size effects on droplet breakup at similar Weber numbers. An upcoming campaign is presented that will expand upon this work with the addition of data on shock droplet interaction with a variable acceleration shock-expansion system.

Deformation and breakup Models

The deformation of a droplet is usually characterized by the ratio of cross-stream droplet diameter to the volume-averaged diameter(or initial diameter). Various empirical models based on experiments ([4], [5], [6], [7]) and theoretical/semi-analytical models have been proposed over the years to predict the instantaneous deformation (as a function of time). O'Rourke and Amsden [8] modeled the deforming droplet as a mass-spring system and proposed a second-order differential equation with constant coefficients called the Taylor Analogy Breakup model, refereed here as original TAB (OTAB). Thereafter several researchers (for instance,[9], [10]) tried to improve the predictions from the TAB model by changing the coefficients of the equation.

Ibrahim et al. [11] considered the conservation of energy of the deforming droplet and proposed the Deformation and Breakup Model(DDB). Stefanitsis et al. [12] have given a comprehensive review of several existing droplet breakup models and proposed their own improvement of the TAB model by making the coefficients Weber number dependent. This is referred to here as the Improved TAB (ITAB) model. They also presented a unified way of representing various analytical models of droplet breakup (see eqn. (**??**)) as a second order non-linear differ-

Table 1. Parameters for different breakup models in unified deformation model [12]

	OTAB	ITAB	DDB
f_{sk}	1	1	1
f_v	$4y^2C_d$, $C_d = 5$	$4y^2C_d$, $C_d = 10$	$9\pi^2$
f_{st}	$8C_k$, $C_k = 8$	$8C_k$, $C_k = f(We)$	$\frac{27\pi^2}{2}$
f_{pr}	$4C_f$, $C_f = 1/3$	$4C_f$, $C_f = g(We)$	$\frac{9\pi}{8}$
$\frac{dS^*}{dy}$	$y - 1$	$y - 1$	$(1 - 2y^{-6})y$
${u^*_{rel}}^2$	1	1	1

Table 2. Weber number dependent coefficients for ITAB model of [12]

C_k	$-1.32 + 0.12We, \quad We \leq 20$ $7.87 - 0.13We, \quad 20 < We < 60$ $0, \quad We \geq 60$
C_f	$0.13 + 0.0026We, \quad We \leq 20$ $0.46 + 0.0022We, \quad We > 20$

ential equation which evolves non-dimensional deformation (y) with respect to non-dimensional time (t^*).

$$y = \frac{d}{d_0} \ , t^* = \frac{t}{t_c} \ , t_c = \frac{d_0}{V_g}\sqrt{\frac{\rho_p}{\rho_g}} \tag{1}$$

$$f_{sk}\ddot{y} + \frac{1}{2}\frac{df_{sk}}{dy}\dot{y}^2 + f_v\frac{Oh}{\sqrt{We}}\frac{\dot{y}}{y^2} + \frac{f_{st}}{We}\frac{dS^*}{dy} = f_{pr}{u^*}^2_{rel} \tag{2}$$

In equation (2), We and Oh are Weber number and Ohnesorge number respectively. Table 1 gives the parameters for the three deformation models, OTAB, ITAB and DDB, used to compare the experimental results in this work. Most empirical or theoretical models give a critical deformation ranging from 1.5 to 2.1 for the initiation of breakup. In the TAB model, breakup starts once $y = y_{cr} = 1.5$ and in DDB the critical deformation is $y_{cr} = We/(12\pi)$.

For the complete characterization of breakup, the initiation time, the breakup end time, child droplet size and rate of child generation (or rate of mass loss of parent drop) need to be modeled. Both TAB and DDB can be used to completely describe the deformation and breakup process or they can be used in conjunction with other breakup models like the wave model [13]. When used with other breakup models, the deformation is used for the calculation of dynamic drag as in Liu et al. [14]. In this paper, we are concerned with the deformation and breakup initiation time rather than full characterization of breakup process so we leave out the description and discussion of breakup models.

Simulation Work

Detailed numerical simulations of an n-Dodecane liquid fuel droplet impacted by a Mach 5 shock were performed to study droplet deformation.

Numerical Method

2D axisymmetric inviscid equations were solved for both the gas and liquid phases. The single species Euler equation represented each phase, which included thermal diffusion effects. The governing equations can be seen below in (3)-(5).

$$\frac{\partial\rho}{\partial t} + \frac{\partial(\rho u)}{\partial x} + \frac{\partial(\rho v)}{\partial y} + \eta\frac{\rho v}{y} = 0 \tag{3}$$

$$\begin{aligned}\frac{\partial(\rho u)}{\partial t} + \frac{\partial(\rho u^2 + p)}{\partial x} + \frac{\partial(\rho vu)}{\partial y} + \eta\frac{\rho vu}{y^\eta} = 0\\ \frac{\partial(\rho v)}{\partial t} + \frac{\partial(\rho uv)}{\partial x} + \frac{\partial(\rho v^2 + p)}{\partial y} + \eta\frac{\rho v^2}{y^\eta} = 0\end{aligned} \tag{4}$$

$$\begin{aligned}\frac{\partial(\rho E)}{\partial t} + \frac{\partial(u(\rho E + p))}{\partial x} + \frac{\partial(v(\rho E + p))}{\partial y}\\ +\eta\frac{v(\rho E + p)}{y^\eta} = -\frac{\partial q_x}{\partial x} - \frac{1}{y^\eta}\frac{\partial(y^\eta q_y)}{\partial y}\end{aligned} \tag{5}$$

In the above equations, the variable $\eta = 0$ or 1 selects 2D Cartesian or axisymmetric coordinates respectively. The gas phase consists of pure oxygen gas, with specific heat capacity C_p modeled using NASA7 temperature polynomials [15, 16] and thermal conductivity using Sutherland's law [16]. The liquid phase consists of pure n-Dodecane, and was modeled as a stiff fluid using Tait's equation of state 6 with relevent coefficients provided in Table 3.

$$\frac{p + B}{p_\infty + B} = \left(\frac{\rho}{\rho_\infty}\right)^N \tag{6}$$

In (6), B and N are constants, and p_∞ and ρ_∞ are reference pressure and density, respectively. The liquid fuel properties were taken to be constant, independent of temperature variations within the liquid. They were evaluated as the n-Dodecane properties at $T_{avg} = 0.5(T_0 + T_{crit})$, where T_0 is the initial temperature of the liquid in the simulation and T_{crit} is the critical temperature of liquid n-Dodecane.

$B(GPa)$	$p_\infty(Pa)$	$\rho_\infty(kg/m^3)$	N
0.199	1.0×10^5	516.50	7.15

Table 3. Properties for liquid n-Dodecane .

The governing equations detailed in (3)-(5) were solved using IMPACT [17, 18]. IMPACT is a massively parallel, multiphase, shock physics code that uses the finite volume approach. In order to achieve higher order spatial accuracy, a fifth-order Weighted Essentially Non-Oscillatory (WENO) scheme [19] is applied in a direction-by-direction manner to reconstruct cell-face quantities from their cell-centered counterparts. To compute intercell fluxes, the Lax-Fredrich (LF) method [20] is utilized, while the parabolic terms are handled through a second-order central differencing scheme similar to [21]. A third-order Total Variation Diminishing Runge-Kutta (TVD-RK3) scheme is used for time integration [22, 21]. The Level Set Method (LSM), specifically the fast local LSM [23], was implemented to track the interface between the two phases. Lastly, a Riemann Solver-based Ghost Fluid Method (RS-GFM) [17, 24, 21] was used to establish the coupling between the two phases.

Initial Conditions

In this work, we simulate an inert (non-reacting, non-evaporating) flow case for a 2D axisymmetric liquid fuel droplet impacted by a Mach 5 shockwave. The simulation setup can be seen in Figure 1. A zero gradient boundary condition was implemented along all of the boundaries except for the axis of symmetry. The simulation was run with a mesh resolution of 512 cells per diameter (CPD). The n-Dodecane fuel droplet had an initial diameter of 5 $[\mu m]$ and was preheated to a temperature of 460 [K]. The gas phase, consisting of pure O_2 at 1 [atm] pressure, was preheated to a value of 700 [K]. Both liquid fuel and oxidizer were preheated as this is known to increase the combustion efficiency in detonation engines [25, 26, 27]. To achieve a Weber number of 500 in the post-shock flow, the surface tension coefficient was adjusted to $\sigma = 0.1496$ $[N/m]$. The simulation was run to a non-dimensional time $t^* = 1$.

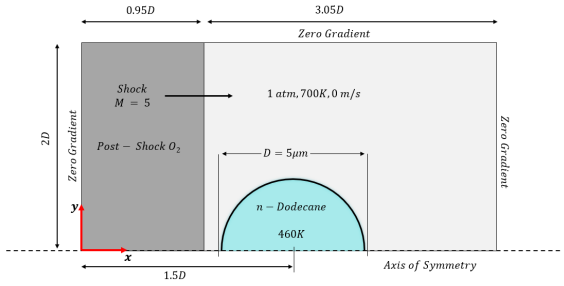

Figure 1. Schematic for 2D axisymmetric shock-droplet simulation [18].

Droplet Morphology and Deformation Results

Numerical schlieren images are presented in Figure 2 at different t^* values throughout the simulation to show the evolution of the droplet interface and surrounding flow field. The interface contours used for deformation measurements are shown in red. The OTAB deformation model [28] was used to predict droplet deformation to compare with calculated deformation from simulation data.

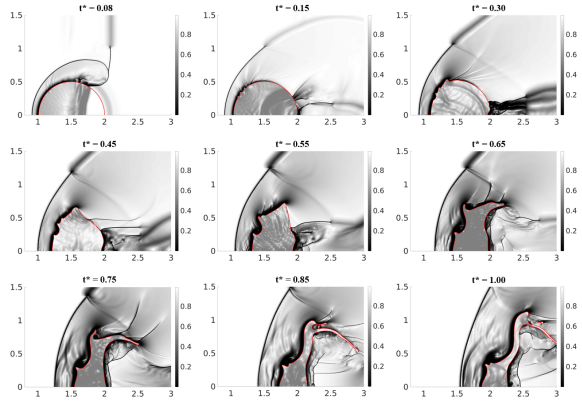

Figure 2. Numerical Schlieren of Mach 5 shock wave impacting 5 μm n-Dodecane liquid droplet.

As the shock wave travels across the droplet, a compression wave travels within the droplet starting from the windward side. The compression wave reflects as it reaches the leeward side and forms an expansion wave, seen in the schlieren image at $t^* = 0.15$ in Figure 2. As the droplet deforms, the continuous reflection of compression and rarefaction waves from the deformed droplet interface, results in the complex structure of pressure wave oscillations inside the liquid droplet, as visible in the schlieren images. Kelvin-Helmholtz (KH) instability waves begin to appear on the droplet surface around $t^* = 0.15$. The KH waves begin to elongate and are drawn downstream into thin filaments around $t^* = 0.65$. These filaments then start to shear from the droplet's surface at $t^* = 0.75$, forming elongated thin sheets. As the shock wave moves across the interface, a recirculation region begins to form on the leeward side of the droplet. A detached bow shock is observed upstream of the droplet which shows the presence of supersonic post-shock gas velocity. The elongated sheet structures dominate late-time droplet behavior and drag, while early time droplet morphology conforms largely to an elliptical shape.

We define the droplet deformation rate as $d(t)/d_0$, where d represents the $y-$diameter of the

best fitting ellipse to the droplet at that time. To obtain $d(t)$, we first obtain $d_x(t)$ the horizontal diameter of the ellipse fitting the observed level set surfaces from the simulations. Then, requiring the distorted ellipse at time t to have the same volume as its initial counterpart of diameter d_0, the $y-$ diameter can be computed using (7). The vertical diameter computed $d(t)$ in this manner can be compared directly with predictions from the OTAB model, which assumes the droplet deforms from an initial sphere into an axisymmetric ellipsoid, while conserving volume.

$$d(t) = \sqrt{\frac{d_0^3}{d_x(t)}} \tag{7}$$

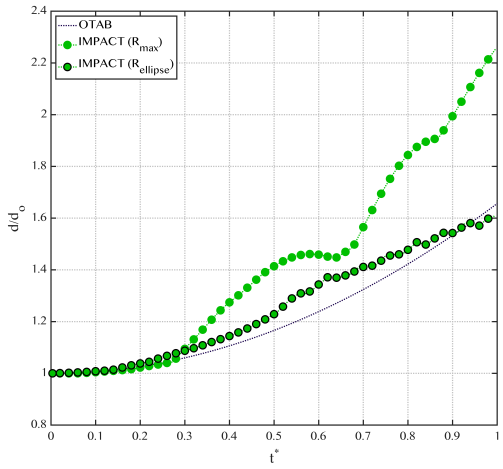

Figure 3. Comparison of deformation rate for simulation (obtained using d_{max} and the ellipse-fitting method) and OTAB model predicted data for a 5 μm droplet at Mach 5, We = 500.

In Figure 3, we plot the deformation rate $d_y(t)/d_0$ obtained from the DNS data (processed using the ellipse fitting method described above), and the corresponding predictions from the OTAB model [8]. We also plot $d_{max}(t)/d_0$, where $d_{max}(t)$ was obtained as the maximum y-diameter of the level set surface at t^*. For $t^* < 0.18$, all three methods are in good agreement, as the droplet stays largely elliptical (see Figure 2). For $t^* > 0.18$, some discrepancy between the DNS and OTAB model is observed and attributed to the development of KH instability waves (seen on the droplet surface in the schlieren images in Figure 2). At late times ($t^* > 0.5$), oscillations are observed in the simulation data, and are likely due to the thin KH filaments separating from the parent droplet. Results from OTAB model in Figure 3 compare well with the simulation data until the KH-driven sheet structures become prominent at late times.

In Figure 3, we also plot the diametric deformation obtained from the d_{max} measure. For $t^* < 0.3$, d_{max} is in agreement with IMPACT data, corresponding to the initial spherical phase of droplet growth. For $t^* > 0.3$, d_{max} shows the fastest droplet deformation, since it accounts for the maximum extent of the evolving thin filaments. The decrease in d_{max} around $t^* = 0.55$ is due to the ejected KH sheets growing radially initially and then being entrained into the post-shock flow and towards the leeward end of the droplet. Since the d_{max} measure is dominated by the KH sheets at late times, it appears to follow a different power-law behavior than the essentially core-deformation measure of d_y. This will be investigated in future studies.

Experimental Procedures and Methodology

Shock Tube Facility

The experimental work utilizes a shock tube facility to create a shock environment with prescribed pressure and velocity gradients to interact with a single droplet, see figure 4. This facility generates a mechanically induced shock wave by utilizing compressed nitrogen into standard pressure and temperature atmospheric air. The shock tube consists of three interconnected sections: (1) the driver section, which stores high-pressure gas to initiate and sustain the shock wave; (2) the driven section, where the shock wave develops into a planar shock; and (3) the test section, where the shock wave interacts with the single droplet and the morphological evolution is captured through imaging techniques. The driver and driven sections are separated by a diaphragm, which is ruptured to initiate the shock. The diaphragm is cut by an "X-shaped" knife located immediately downstream of it to guarantee consistent and repeatable shock initiation. This diaphragm is designed to rupture rapidly when necessary, and the strength of the shock wave can be modulated by using more durable diaphragms to generate the shock. Upon rupture of the diaphragm, compressed gas from the driver section is expelled into the driven section. For this study, three shock conditions have been selected by utilizing 0.254 [mm]and 0.762 [mm] polycarbonate diaphragms, and a 24 gauge (0.51 [mm]) galvanized steel sheet-metal diaphragm to generate post-shock gas velocities of $180[m/s]$, $270[m/s]$ and $470[m/s]$ respectively. For more detail, on the shock-tube facility and operation, please see [29].

A single monodispersed droplet is created with

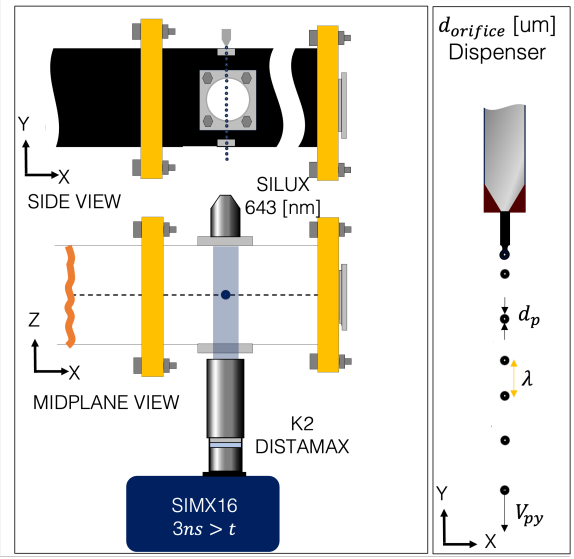

Figure 4. Experimental Facility

a vibrating dispensing needle from the MICROFAB model $MJ - Aof60[\mu m]$. The droplet size is controlled by the needle diameter, liquid velocity (driven by the needle's backpressure), and frequency. In order to decrease droplet-droplet interactions, the distance between the droplets is maximized by utilizing higher frequencies and velocities. The dispensing pressure is set to 300 [mmHg] providing a downward droplet velocity of $\sim 6.5[m/s]$. The size distribution of droplets produced was extensively characterized via high-speed shadowgraph microscopy. Acetone is utilized in this study because its thermophysical properties are similar to fuels such as n-Dodecane while also having a high vapor pressure, driving more rapid evaporation. This makes it an excellent fluid to study high We droplet breakup and vaporization.

For the initial conditions, Acetone droplets are injected a few seconds before the shock wave reaches the test section, preventing a high level of evaporation of the droplet liquid before the experiment. In order to enter the shock tube, liquid passes through an orifice hole of diameter $\sim$ 1.5 [mm], and exits a 3/8 [in] diameter hole to prevent over-pressure into the orifice. This system provides reliable and well-defined initial conditions at the start of an experiment.

The development of the droplet morphology is captured utilizing a SIMX 16 camera with a Distamax K-2 long-distance microscope and a high-power SI-LUX burst laser at 643 [nm], offering a distortion-free image of the droplets. The SIMX 16 camera records 16 images with adjustable frame exposure and delay between successive images. For the present experiments, a $10 \pm 2ns$ exposure time was used. The magnification power is chosen such that the system has enough resolution to resolve the droplets and their wave structures. For the 150 um droplets, a magnification power of $\sim$ 11.5 providing a FOV of 550 x 700 $[\mu m]$ was selected, providing a resolution of $\sim 0.55\mu m$ per pixel.

$d_p[\mu m]$	$V_g[m/s]$	M	W_e
158	$\sim$ 180	1.357	395
158	$\sim$ 270	1.566	1095
158	$\sim$ 470	2.095	4899

Imaging Processing

A MATLAB edge-boundary detection algorithm is used to obtain the droplet growth rate. Initially, the algorithm takes a region of interest three times bigger than the droplet based on the original reference particle location. Next, a Gaussian smoothing filter is applied to eliminate spurious noise and then a binary image is generated. The sensitivity of this binary process was adjusted to ensure accurate detection of droplet morphology. A boundary tracing built-in function is used to identify the maximum particle boundaries in the X and Y directions. After analyzing all images, the deformation rates (the ratio of the maximum to the initial particle diameter, d/d_0) are estimated.

Once the experimental results are obtained, image sizing data are transformed from pixels to $[\mu m]$ to confirm the initial particle diameter and calculate the shock reference to the leading edge of the droplet. Every experimental time is offset from the shock arrival. The experimental times are then normalized with the characteristic breakup time as shown in eqn 1.

Deformation Experimental results

Experimental results of the single acetone droplet experiment at three different pressures and velocities are shown table and in figures 7,8 and 9. The initial droplet velocity before the shock is estimated to be $V_g \sim 0$. As the shock traverses the droplet, the deformation process starts. The rate of deformation obtained from the experimental results increases slightly with an increase of Weber numbers, see figure 5. However, there is not a strong dependency of the deformation rate on the Weber number in the cases presented here.

From $0 < t^* < 0.225$, the deformation rate is not a function of Weber number. At later times, the deformation rate increases slightly with increasing velocity. This departure could be an indication of the

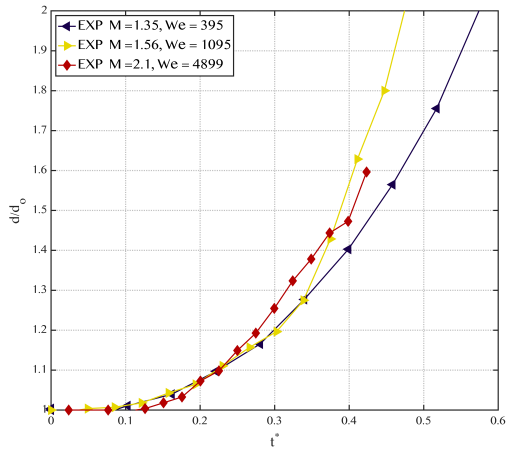

Figure 5. Experimental results of the deformation rate for a 158 um droplet

We	M	Breakup initiation (t^*)	Deformation at breakup (d/d_o)
395	1.357	$0.517 - 0.577$	< 2.01
1095	1.566	$0.339 - 0.375$	< 1.43
4899	2.095	$0.324 - 0.35$	< 1.38

breakup initiation which can be seen to start more rapidly when there is a shearing of droplet edges, as shown in figures 7, 8 and 9. Table provides breakup initiation times and total deformation for each of the cases studied.

Deformation rates comparison

The overall comparison of the deformation rate has been considered by including the deformation rate of large droplet work from [3], and the experimental and simulation of small droplets presented in this work. It can be seen in figure 6 that the droplet deformation rate decreases with particle size. In other words, the smaller the particle the faster the particle response time and the slower the deformation rate.

When comparing the results to existing deformation models, it's not evident which model accurately captures the physical characteristics of the deformation process. The OTAB model performs better in predicting droplet deformation rates as particle size decreases. However, it deviates from accurate predictions as particle size increases. The ITAB model closely predicts the deformation rate within its model validity range when compared to experimental data. However, it significantly underpredicts the deformation rate outside these expected conditions. Additionally, the model's performance at similar conditions, does not seem to capture the rate of very small particle size. The DDB model shows a similar deformation rate to the experiments but it has distinct offset.

Conclusions

The result presented here represent a work in progress, but highlight the dynamics of small droplets at high Weber numbers. The deformation of small ($\sim 150\mu m$) droplets is explored at high spatial (300 pixels per diameter) and temporal (down to 100ns interframe times) resolutions. The deformation of smaller droplets is obtained from high-fidelity DNS of $\sim 5\mu m$ droplets at high Mach numbers (M¿5).

The results here show that Weber number does not fully describe the deformation rate on its own. We observe a diameter dependence with larger droplets deforming faster than smaller droplets. The deformation process is highly dependent on the droplet dynamics. As the droplet size decreases the particle response time decreases and the droplet dynamics influence the rate of deformation. The ITAB model shows faster deformation with increasing Weber number, capturing some of the behavior observed here, but it overpredicts deformation rates, and cannot capture the size effects independent of We.

Further improvements to deformation models may need to consider the time-dependent gas velocity as a function of the particle response time. Future experimental and simulation work will seek to bridge the length-scale difference, exploring smaller droplets ($\sim 50\mu m$) at high Mach numbers (M¿2.0). Additionally, we will seek to understand the role of the changing relative gas conditions by exploring prescribed time dependent gas conditions using a coupled shock-expansion wave system.

Acknowledgement

This work was partially supported by a grant from the National Science Foundation (grant Nos. 1933479, 2053154, and 2332917).

Submission

Papers must be submitted through the website www.openconf.org/ILASS2023.

References

[1] M Pilch and CA Erdman. *International journal of multiphase flow*, 13(6):741–757, 1987.

[2] K. Mizuno, T. Yada, T. Kamiya, M. Asahara, and T. Miyasaka. *International Journal of Multiphase Flow*, 155:104141, 2022.

[3] Sergey V. Poplavski, Andrey V. Minakov, Anna A. Shebeleva, and Viktor M. Boyko. *International Journal of Multiphase Flow*, 127:103273, 2020.

[4] BE Gel'Fand, SA Gubin, and SM Kogarko. *Journal of engineering physics*, 27:877–882, 1974.

[5] L.-P. Hsiang and G.M. Faeth. *Int. J. Multiphas. Flow*, 18(5):635–652, 1992.

[6] W-H Chou and GM Faeth. *International journal of multiphase flow*, 24(6):889–912, 1998.

[7] Hui Zhao, Hai-Feng Liu, Jian-Liang Xu, Wei-Feng Li, and Kuang-Fei Lin. *Physics of Fluids*, 25(5), 2013.

[8] Peter J O'Rourke and Anthony A Amsden. The tab method for numerical calculation of spray droplet breakup. Technical report, SAE Technical Paper, 1987.

[9] Björn Andersson, Valeri Golovitchev, Stefan Jakobsson, Andreas Mark, Fredrik Edelvik, Lars Davidson, and Johan S Carlson. *Journal of Mechanical Engineering and Automation*, 3(2):54–61, 2013.

[10] Kyle A Daniel, Daniel R Guildenbecher, Paul M Delgado, Glen E White, Sam M Reardon, H Lee Stauffacher III, and Steven J Beresh. *AIAA Journal*, 61(6):2347–2355, 2023.

[11] EA Ibrahim, HQ Yang, and AJ Przekwas. *Journal of Propulsion and Power*, 9(4):651–654, 1993.

[12] Dionisis Stefanitsis, George Strotos, Nikolaos Nikolopoulos, Emmanouil Kakaras, and Manolis Gavaises. *International Journal of Heat and Fluid Flow*, 76:274–286, 2019.

[13] Jennifer C. Beale and Rolf D. Reitz. *Atomization and Sprays*, 9(6):623–650, 1999.

[14] Alex Liu, Daniel Mather, and Rolf Reitz. *SAE Technical Paper 930072*, p. 17, 03 1993.

[15] Bonnie J. McBride, Michael J. Zehe, and Sanford Gordon. Nasa glenn coefficients for calculating thermodynamic properties of individual species. Technical report, Cleveland, Ohio, 2002.

[16] Benjamin J. Musick, Manoj Paudel, Praveen K. Ramaprabhu, and Jacob A. McFarland. *Combustion and Flame*, 257:113035, 2023.

[17] P. Bigdelou, C. Liu, P. Tarey, and P. Ramaprabhu. *Computers and Fluids*, 233:105250, 2022.

[18] P. Tarey, P. Ramaprabhu, and J.A. McFarland. *International Journal of Multiphase Flow*, 174:104744, 2024.

[19] C.W. Shu. *High-Order Methods for Computational Physics*, chapter High Order ENO and WENO Schemes for Computational Fluid Dynamics. Springer, 1999.

[20] E.F. Toro. *Riemann Solvers and Numerical Methods for Fluid Dynamics: A Practical Introduction*. Springer, 2009.

[21] R.W. Houim and K.K. Kuo. *Journal of Computational Physics*, 235:865–900, 2013.

[22] S. Gottlieb and C.W. Shu. *Mathematics of Computation*, 67:73–85, 1998.

[23] D. Peng, B. Merriman, S. Osher, H. Zhao, and M. Kang. *Journal of Computational Physics*, 155:410–438, 1999.

[24] P. Das and H.S. Udaykumar. *Journal of Computational Physics*, 405:109005, 2020.

[25] S. Jin, C. Xu, H. Zheng, and H. Zhang. *Proceedings of the Combustion Institute*, 39:4761–4769, 2023.

[26] P. Wolanski, W. Balicki, W. Perkowski, and A. Bilar. *Shock Waves*, 31:807–812, 2021.

[27] C. Yan, W. Nie, B. Wang, and W. Lin. *AIP Advances*, 13:065127, 2023.

[28] P J O'Rourke and A A Amsden. 1, 1 1987.

[29] Vasco Duke-Walker, Benjamin J Musick, and Jacob A McFarland. *International Journal of Multiphase Flow*, 161:104389, 2023.

Appendix

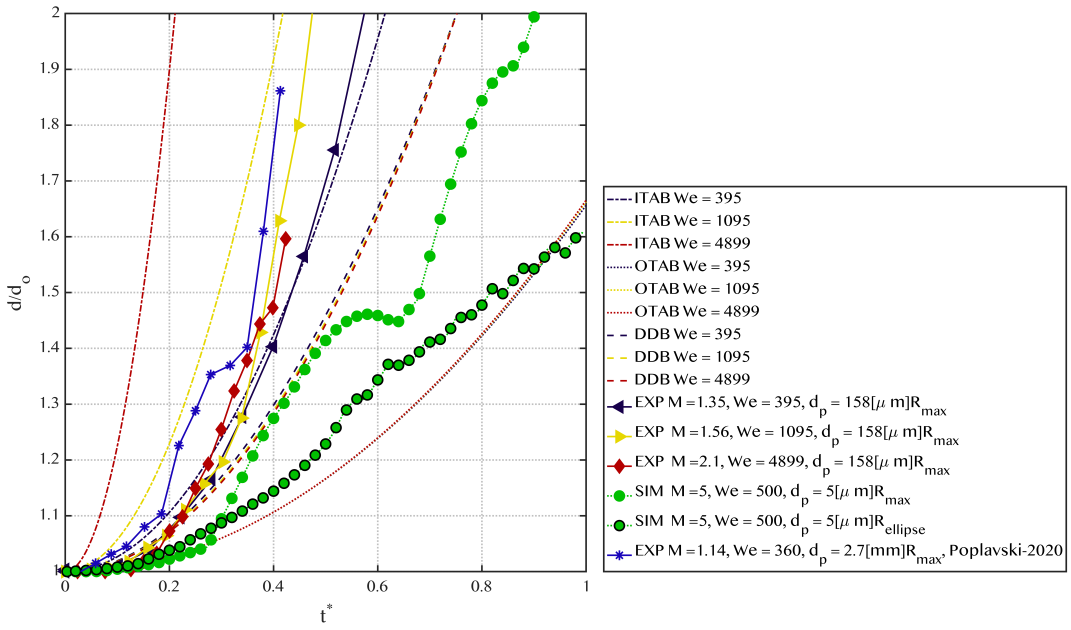

Figure 6. Simulation and experimental deformation rates compare to models

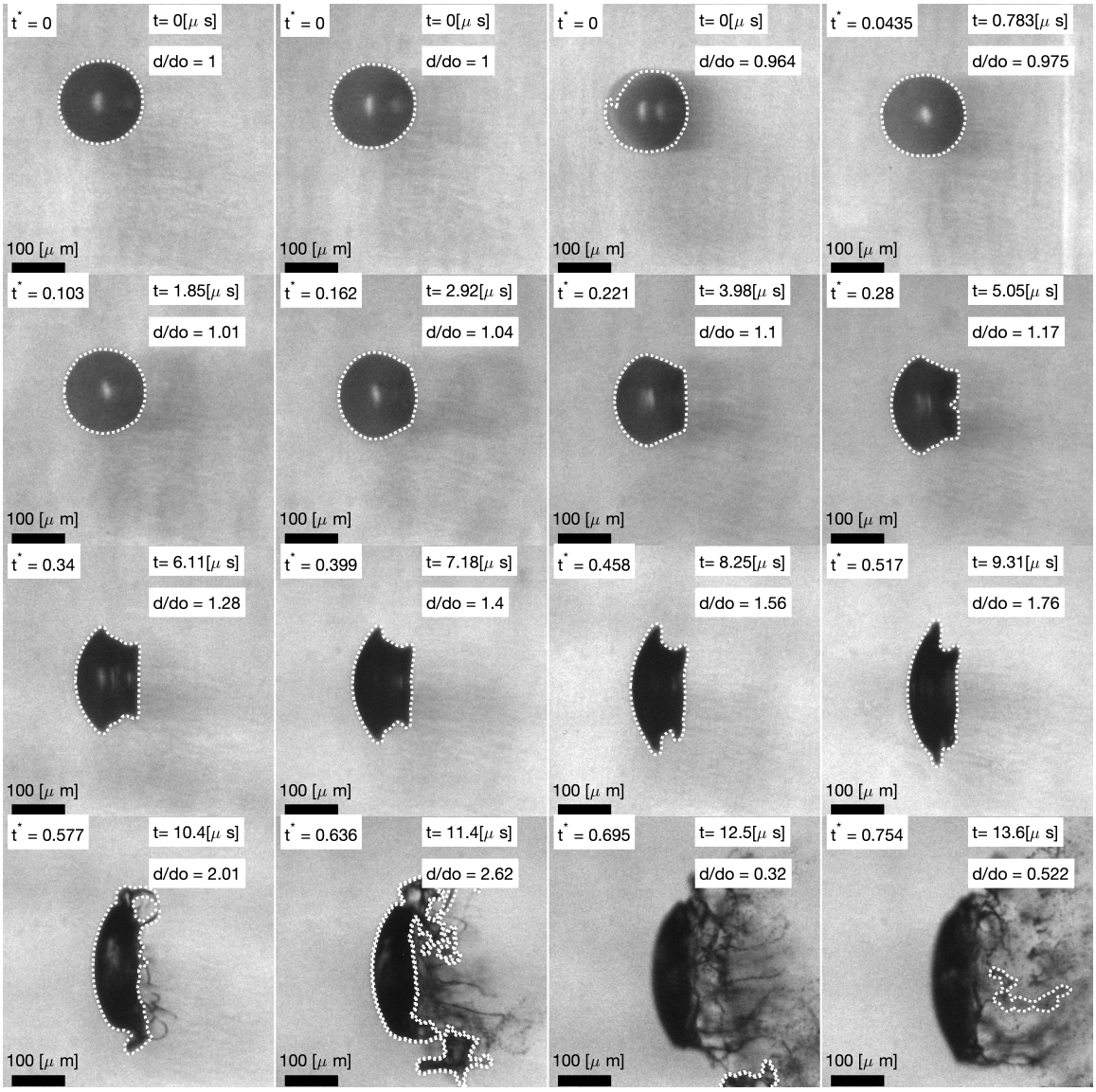

Figure 7. Experimental results of the deformation rate for a 158 um droplet at Mach 1.357, We = 395

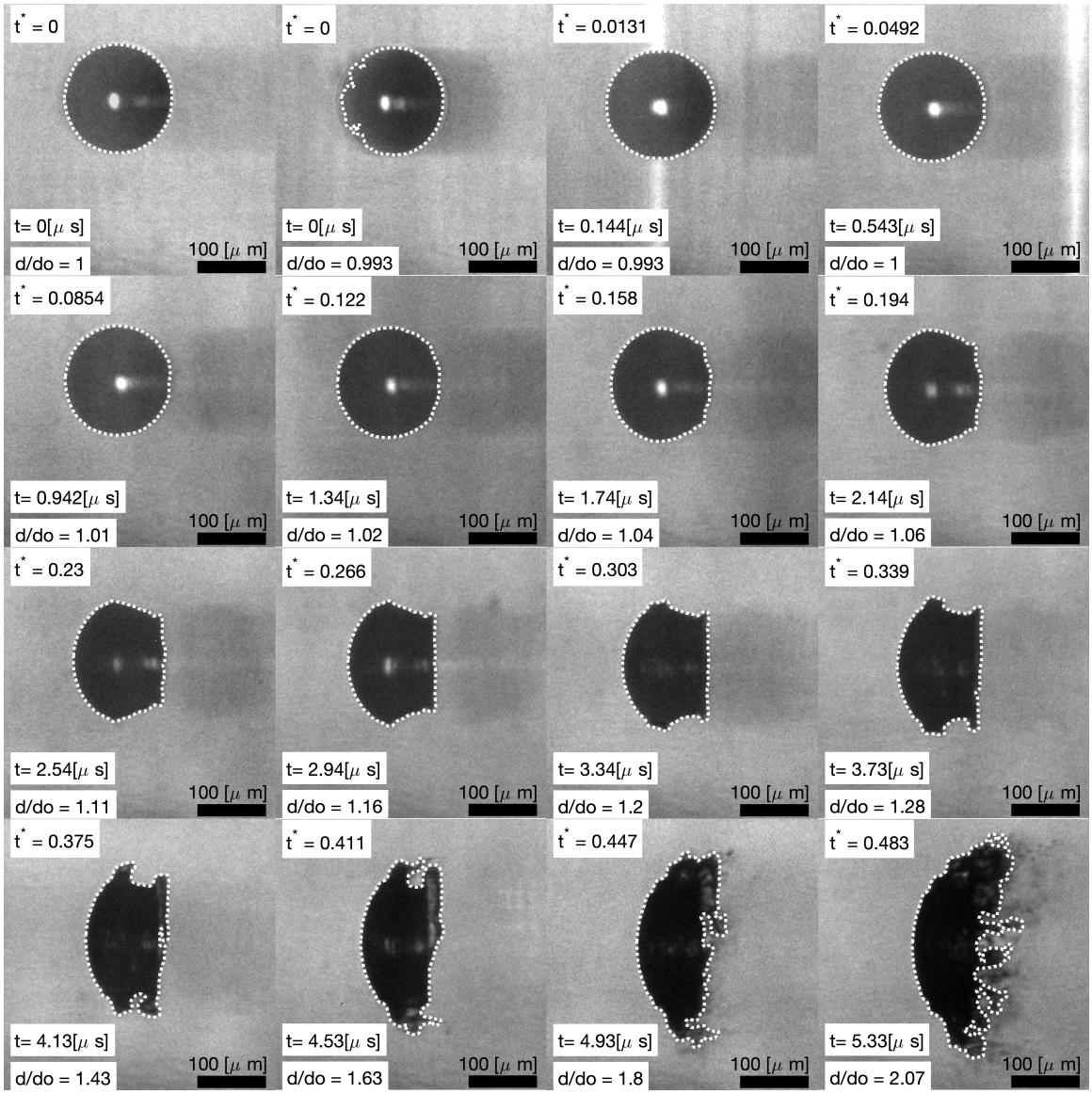

Figure 8. Experimental results of the deformation rate for a 158 um droplet at Mach 1.566, We = 1095

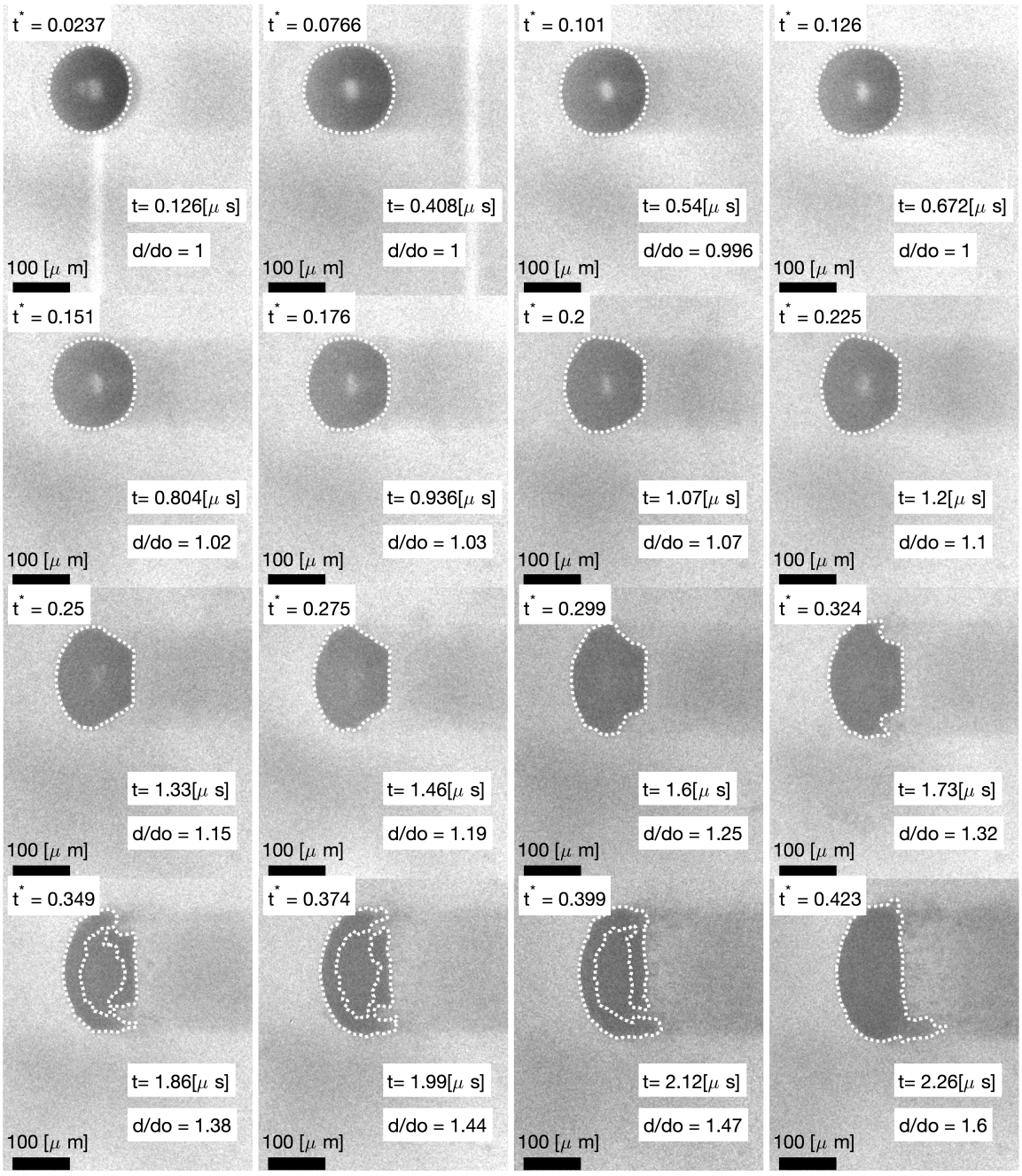

Figure 9. Experimental results of the deformation rate for a 158 um droplet at Mach 2.095, We = 4899